Kinetic and microstructural studies on the devitrification of $Fe_{60-x}Co_{18}Mn_xNb_6B_{16}$

amorphous alloys

H. Benaini, J.S. Blázquez, C.F. Conde, A. Conde

Departamento de Física de la Materia Condensada. ICMSE-CSIC. Universidad de

Sevilla. P.O. Box 1065. 41080 Sevilla, Spain.

Abstract: Kinetic and microstructural studies have been performed on $Fe_{60-x}Co_{18}Mn_xNb_6B_{16}$ (x=0, 2, 4) alloy by using different techniques. Isothermal and non isothermal kinetics agree describing the nanocrystallization as a strongly impinged growth process. Developed microstructure is similar for all the studied alloys. Nanocrystals are irregularly shaped, ~20 nm in size, and formed by agglomerates of smaller and more regular units of ~5 nm diameter. From the present data it is not possible to totally exclude the presence of Mn atoms inside the crystals. However, a preferential partition of this element into the residual amorphous matrix is clearly derived from Mössbauer results.

Keywords: A-Nanostructured materials, C-kinetics, C-microstructure, D-Mössbauer spectroscopy.

*Corresponding author: Prof. A. Conde

Departamento de Física de la Materia Condensada. Universidad de Sevilla.

Apartado 1065, 41080 Sevilla (Spain).

Phone: (34) 95 455 28 85

Fax: (34) 95 461 20 97

E-mail: conde@us.es

1.   Introduction

Nanocrystalline Fe-based alloys are interesting materials not only from a

fundamental point of view, due to their metastable two-phase microstructure, but also

due to their technological applicability exhibiting outstanding soft magnetic properties:

very low coercivity, high saturation magnetic flux and high permeability [1].This is due

to the averaging out of the magnetic anisotropy of the crystalline phase as the exchange

length becomes larger than the structural length. However, this is valid only below the

Curie temperature of the amorphous matrix, which transmits the exchange interaction

between nanocrystals [2], establishing a temperature limit in the application of these

systems.

A successful and widely used technique to obtain nanocrystalline alloys is the

controlled partial crystallization of a precursor amorphous alloy with suitable

composition. In this sense, the Fe-based nanocrystalline alloys can be classified into two

groups [1]: FINEMET-type alloys, developed from ternary Fe-Si-B amorphous alloys

after small addition of Nb and Cu, and NANOPERM-type alloys, developed from the

eutectic Fe-B composition after addition of an early transition metal as Zr, Nb, Hf, etc.

In both families, the early transition metal atoms, due to their very low solubility in the

α-Fe phase, are expelled out of the forming nanocrystals to the residual amorphous

matrix, piling up at the boundary between the two phases due to their very slow

diffusivity in the amorphous matrix, and blocking the growth of the crystallites. Cu is

necessary in FINEMET alloys in order to enhance the nucleation via Cu-clustering

phenomenon. However, in NANOPERM alloys, Cu addition is not essential, although it

refines the nanocrystalline microstructure [1].

In 1998, HITPERM alloys appeared after the partial substitution of Co for Fe in

NANOPERM-type alloys [3]. The main effect of this compositional change is the huge

increase of the Curie temperature of the amorphous matrix extending the temperatures

of applicability of these nanocrystalline soft magnetic alloys to higher values than those

achieved by their Co-free counterparts. Partial substitution of Co for Fe in FINEMET

alloys has attracted also great interest in the last years [4,5,6]. Although similar results

were found, the presence of Si inside the nanocrystals reduces the Curie temperature of

the α-Fe phase with respect to HITPERM alloys.

Most recently, the effect of Mn on the nanocrystalline Fe-based alloys is a

subject of interest in FINEMET [7,8,9,10], NANOPERM [11,12] and HITPERM

[13,14,15] alloy families. The aim of this work is to analyze the effect of small

additions of Mn in the microstructure and magnetic properties of a $Fe_{60-x}Co_{18}Mn_xNb_6B_{16}$ alloy series.

2   Experimental

Amorphous ribbons with nominal compositions $Fe_{60-x}Co_{18}Mn_xNb_6B_{16}$ (x=2, 4),

about 30 μm thick and 1 cm wide, were prepared by planar flow casting. The

amorphous character of the as-cast alloys has been checked by X-ray diffraction. In

order to produce samples with different microstructures, as-cast ribbons were heated up

to selected temperatures at 10 K/min in a lamp furnace under inert atmosphere.

Differential scanning calorimetry (DSC) was performed in a Perkin-Elmer DSC-7 under

argon atmosphere and thermomagnetic gravimetry (TMG) in a Perkin-Elmer TGA-7

applying the magnetic field of a small magnet (~20 mT). Microstructure was studied by

X-ray diffraction (XRD) at room temperature using Cu-Kα radiation; transmission

electron microscopy (TEM) in a Philips CM200 operated at 200 kV and Mössbauer

spectroscopy (MS) at room temperature in a transmission geometry using a [57]Co(Rh)

source. The incident γ-beam was perpendicular to the ribbon plane. Values of the

hyperfine parameters were obtained by fitting with NORMOS program [16]. The

isomer shift, I, was quoted relative to the Mössbauer spectrum of an α-Fe foil at room

temperature. Spectra of amorphous samples were fitted using a distribution of hyperfine

fields, HF. In the case of nanocrystalline samples, a set of discrete values of hyperfine

fields and two hyperfine field distributions were used to fit the experimental data. The

two hyperfine field distributions would roughly correspond to the amorphous phase and

the interface region. The distinction between the limits of hyperfine fields

corresponding to the amorphous and the interface regions is ambiguous and thus

overlapping between them was allowed in the fitting process. In the following, results

will be given as the average between these two contributions as amorphous+interface

contribution.

3.   Results and discussion

3.1   Nanocrystallization kinetics

Figure 1 shows the DSC plots of the 2 and 4 at. % Mn alloys. In both cases, two

devitrification processes are found, as it occurs for the Mn-free composition [17]. The

peak temperature, T_p, of the first exotherm increases as the Mn content in the alloy

increases but that of the second event does not show the same trend for the studied

alloys. The enthalpy, ΔH, of the first process is independent of the Mn content.

However, a slight decrease of ΔH for the second transformation stage is observed. Table

1 summarizes the devitrification parameters of the studied alloys.

The devitrification process can be also followed from TMG data. Figure 2 shows

the temperature dependence of low field magnetization, M, for as-cast samples. A first

fall to zero of M is due to the ferromagnetic-paramagnetic transition of the amorphous

phase. The rise in M above 700 K is due to the formation of ferromagnetic nanocrystals,

in agreement with the crystallization onset temperatures obtained from DSC. Below

1000 K a new fall in *M* occurs not reaching zero. This fall does not correspond to a

Curie transition but to a recrystallization process ascribed to the second transformation

stage detected by DSC, as it was observed for the Mn-free alloy [18]. A zero *M* value is

not obtained in the temperature range explored, as the Curie temperature of the

α-FeCo(Mn) nanocrystals should be higher than 1100 K. A clear effect of Mn on the

Curie temperature of the amorphous alloy (see table 1) is observed with a reduction of

about 20 K/at.% of Mn.

The kinetics of nanocrystallization was studied from both isothermal and non-

isothermal experiments. Isothermal transformation was followed from the TMG signal

registered at different temperatures. As the Curie temperature of the amorphous alloy is

lower than the crystallization onset temperature, a clear signal of the time dependence of

the magnetization, *M(t)*, can be obtained, which can be normalized to its saturation

value to obtain the transformed fraction, *X(t)*. The transformed value was analyzed in

the frame of Johnson-Mehl-Avrami-Kolmogorov (JMAK) theory [19] which supplies a

relationship between X and t as:

$$X(t) = 1 - \exp\left\{-\left[k(t - t_0)^n\right]\right\} \quad (1)$$

where *k* is the velocity factor, t_0 is the induction time and *n* is the Avrami exponent. The

theory predicts the plot of Ln[-Ln(1-*X*)] vs. Ln[*t-t_0*] to be a straight line with slope *n*. A

local Avrami exponent, *n(X)*, can be obtained from the derivative of Ln[-Ln(1-*X*)] with

respect to Ln[*t-t_0*]. The corresponding curves are shown in figure 3 for different

temperatures. In order to obtain the activation energy, *Q*, of the nanocrystallization

process, several isothermal methods were applied. Two averages values can be obtained

after proposing an Arrhenius dependence of *k* and t_0 with the temperature (see table 2).

Besides, it is possible to obtain a local *Q(X)* using the Arrhenius thermal dependence for

the time needed to achieve a certain value of X. The resulting plots are shown in figure

4 showing that Q decreases as X increases as it was observed for the Mn-free alloy [20].

Kinetic information can also be extracted from non-isothermal experiments. Average

values of the nanocrysallization process were obtained after applying three different

methods [21]: Kissinger, Augis-Bennett and Gao-Wang approaches. Kinetic results are

summarized in table 2.

The Ozawa method is another non-isothermal approach which supplies the

Avrami exponent after comparing scans at different heating rates, β, using a modified

JMAK expression for non-isothermal regimes. A $n(T)$ curve can be obtained as the

slope of the plot of $Ln[-Ln[1-X(T)]]$ vs $Ln[1/\beta]$ for a selected temperature T and

different β values. Under this approximation, it is worth noticing that, at a given

temperature for different scanning rates, the process might be in a different stage of

development. Therefore, in this approach, kinetic parameters, as Avrami exponent and

activation energy, are considered independent of X.

Recently, a non-isothermal method has been developed to obtain local values of $n(X)$

from a single DSC scan and an estimation of the activation energy of the process under

the approach of isokinetic transformations [21]. The $n(X)$ curves obtained from DSC

plots at different heating rates collapse as it can be observed in figure 5 for both studied

alloys. Good agreement is found between non-isothermal and isothermal $n(X)$ values

(see figure 3). A good agreement can be also found between the $n(T)$ values obtained

from Ozawa method and those from the isokinetic approach as it is shown in figure 6. In

fact, as Ozawa method intrinsically assumes constant kinetic parameters, the obtained

values have sense only in the range where $n(T)$ is constant, as in the long tails of the

DSC peak. Gao-Wang method also supplies a value of $n\sim1$, calculated at the peak

temperature of the nanocrysallization process ($X\sim0.2$), which agrees with the low

crystalline volume fraction value obtained from both the isokinetic approach and the isothermal results.

All applied kinetic methods agree describing a nanocrysallization process characterized by $Q{\sim}4$ eV and $n{\sim}1$ for low crystalline volume fraction which decreases as the nanocrystallization progresses. Although these n values are too low to be interpreted in the frame of JMAK theory [19], a qualitative interpretation is plausible as a strongly impinged growth process due to the Nb piling up at the edge of the growing nanocrystals.

3.2   Microstructure

Figure 7 shows the XRD pattern of samples heated at 10 K/min up to several temperatures. The α-Fe,Co nanocrysalline phase is not detected at temperatures below the nanocrystallization onset and is the only crystalline phase present for temperatures below the second transformation stage. During this second stage (samples annealed at 1000 K) some boride phases appear, mainly the $(FeCoNb)_{23}B_6$ phase by a recrystallization process [18]. Lattice parameter of the α-FeCo phase, a, was obtained from the 2θ values of (110), (200), (211) and (220) diffraction peaks and the resulting values oscillate into the error bar. The mean grain size of the nanocrystals, $<D>$, was obtained from Scherrer formula and the crystalline fraction was obtained after deconvolution of the (110) crystalline peak and the amorphous halo, and taking into account the different scattering power of the two phases of the system. Results are summarized in table 3. The estimated grain size is 10-12 nm with no significant change with the Mn content or the temperature of treatment. The maximum crystalline volume fraction achieved in the nanocrystallization process is ~60 % for both alloys.

Figure 8 shows TEM bright field images of nanocrystalline and fully crystalline samples. The nanocrystals are not uniformly distributed and a closer view (figure 9) shows that they are very irregular in shape, and look like agglomerates formed by smaller and more regularly shaped crystallite units with the same crystallographic orientation. The size of these smaller units remains almost constant as the nanocrystallization progresses (~5 nm diameter) as it was also observed for the Mn-free alloy [22]. This microstructure, combined with the strongly impinged kinetics, can be interpreted as the competition between two nucleation phenomena and a very strongly impinged spherical growth. This spherical growth corresponds only to the small units forming the agglomerates and saturates at about 5 nm in diameter. The first nucleation phenomenon corresponds to the formation of nuclei in isolated areas, not affected by the depletion in Fe due to neighbor nanocrystals, but which have to overcome the large surface energy formed between the new nucleus and the surrounding amorphous matrix. The second nucleation phenomenon corresponds to the epitaxial germination of new nuclei on an already formed nanocrystal which growth has been blocked and, therefore, with the same crystallographic orientation. In this case the interface energy is strongly reduced but the new nucleus appears in a region poorer in Fe than for the former nucleation mechanism.

The microstructure of amorphous and nanocrystalline samples was also observed using Mössbauer spectroscopy (MS). Figure 10 shows the MS spectra of as-cast samples as well as the hyperfine field (HF) distribution used to fit them. It can be observed that these spectra are formed by very broad sextets which can be fitted using a bimodal distribution of HF, characteristic of amorphous alloys with early transition metals [6]. Also there is a clear reduction of the average hyperfine field with the Mn

content, in agreement with the decrease in the Curie temperature of the amorphous alloys observed by TMG.

At temperatures above the crystallization onset (figure 11 for the MS spectra and figure 12 for the *HF* distributions), the presence of crystals is detected by the appearance of a sharp sextet which external lines do not overlap with the amorphous signal. This sextet becomes more important as the nanocrysallization progresses. However, the lines are too broad to be ascribed to a single Fe site contribution. Therefore, 4 different sites (from 33 to ~37 T) were used. The *HF*>33.0 T are ascribed to Fe atoms in crystalline sites with some Co as near neighbor (nn) (*ΔHF*=2, 3.5 and 4 T for 1, 2 and 3 Co as nn, respectively [23]). The average values of *HF* (35.4 T) and *I* (0.03 mm/s) over these contributions are almost constant as the nanocrystallization progress, pointing a constant composition of the nanocrystals. Neglecting a possible low Mn content into the nanocrystals, average *HF* value yields a Co concentration into the nanocrystals of 16 ± 2 at.% [23], being coherent with the measured value of *I* (with a larger error bar). Co content is close to the 18 at % proposed for the Mn-free alloy [24] and the agreement can be improved taking into account that Mn as nn decreases *HF* of Fe in 2 T [25,26]. Although these data seems to indicate the presence of some Mn atoms inside the nanocrystals, a quantitative estimation of the Mn content is not possible.

It can be observed in figure 12 than the hyperfine field distribution, ascribed to the amorphous+interface contributions, exhibits a low field peak (centered at 5 T for samples at the end of the nanocrystallization) which shifts to lower values as nanocrystallization progresses and becomes more evident as the Mn increases in the alloy. This indicates a clear effect of the Mn on the residual amorphous alloy; therefore, a preferential partition of this element into the residual amorphous matrix is detected. On the other hand, the high field contributions remain and extend to a maximum *HF*

value of the distribution of 32 T. The *HF* values ascribed to the interface region become more distinguishable as the nanocrystallization progresses by two different effect: the amount of atoms in interface increases as the *X* increases and the amorphous contributions shift to lower values of *HF* as the matrix is impoverished in Fe. The *HF*>20 T in the samples heated up to the final stages of the nanocrystallization are ascribed to the interface region with a thickness of ~0.5 nm [27], leading to an average grain size of *<D>*~15 nm, which is of the order of the agglomerates observed by TEM *<D>*~20 nm. The disagreement can be explained as the approximation to obtain the crystal size from MS data assumes spherical crystals and in the studied case they are irregularly shaped and a larger surface yields an underestimation of the grain size. Similar arguments could explain the differences between XRD and TEM results.

Conclusions

Kinetic results based on isothermal (TMG) and non-isothermal (DSC) experiments agree describing a strongly impinged grain growth process characterized by an effective activation energy ~4 eV and an Avrami exponent value ~1 at the early stages of nanocrystallization (*X*<0.2). As nanocrystallization progresses, Avrami exponent decreases to values lower than 0.5.

Microstructure is similar for all the studied alloys. Nanocrystalline microstructure (α-Fe,Co phase embedded in a residual amorphous matrix) is developed during the first crystallization event. Nanocrystals are irregularly shaped ~20 nm in size and formed by agglomerates of smaller and more regular units of ~5 nm diameter. During the second crystallization process, yielding a fully crystalline sample, a recrystallization phenomenon occurs.

Mössbauer spectra of amorphous and heat treated samples at different stages of nanocrystallization show that the effect of Mn is clear on the amorphous phase, but crystalline sites are not affected by its addition to the alloy composition. Although it is not possible from the present data to exclude totally the presence of Mn into the crystalline phase, the preferential partition of this element into the residual amorphous matrix is clearly observed.

Table 1. Curie temperatures (T_C) and crystallization onset (T_O) and peak (T_P)

temperatures and crystallization enthalpies (ΔH) of the two crystallization stages

detected by DSC at 10 K/min.

Alloy x	T_C ±1 (K)	T_o ±0.5 (K)	T_{P1} ±0.5 (K)	ΔH_1 ±10% (J g^{-1})	T_{P2} ±0.5 (K)	ΔH_2 ±10% (J g^{-1})
0 [17]	647	761	775	109	958	15
2	599	780	791	113	976	11
4	569	787	798	106	967	8

Table 2. Average activation energies of the nanocrystallization process of

$Fe_{60-x}Co_{18}Mn_xNb_6B_{16}$ alloys from Kissinger (KIS), Augis-Bennett (A-B), Gao-Wang

(G-W), induction time (t_0) and velocity factor (k) methods.

Mn at.%	Non-isothermal approachs			Isothermal approachs	
	Q(KIS) ± 0.2 (eV)	Q(A-B) ± 0.3 (eV)	Q(G-W) ± 0.2 (eV)	Q(t_0) ± 0.3 (eV)	Q(k) ± 0.5 (eV)
0	3.9 [17]	4.4 [21]	4.4 [21]	3.6 [20]	3.3 [20]
2	4	4.2	4.1	3.8	4.2
4	4.5	4.6	4.4	4.4	4.3

Table 3. XRD results: Lattice parameter (a), mean grain size ($<D>$) and crystalline

volume fraction (X) of the α-FeCo phase of samples heated up to different temperatures

(T_{heat})

Mn (at.%)	T_{heat} (K)	a ± 0.005 (Å)	$<D>$ ± 5 (nm)	X ± 5 (%)
2	786	2.873	10	25
	800	2.862	10	39
	935	2.860	12	61
4	794	2.867	10	26
	810	2.868	12	34
	935	2.862	12	58

Table 4. Mössbauer parameters for crystalline and amorphous plus interface contributions. T_{heat}, maximum temperature of heating; A fraction of Fe atoms; $<H>$, hyperfine field; $<I>$, isomer shift; θ, angle between magnetic moment and radiation beam.

Mn at. %	T_{heat} (K)	Crystalline sites contribution			Amorphous + Interface contributions			θ (°)
		A (%)	$<HF>$ (T)	$<I>$ (mm/s)	A (%)	$<HF>$ (T)	$<I>$ (mm/s)	
0	300	-	-	-	100	22.6	0.034	63.7
	771	16.1	35.2	0.05	83.9	21.9	0.06	48
	787	28.4	35.4	0.04	71.6	21.0	0.06	55
	912	48.9	35.5	0.03	51.1	17.0	0.05	28
2	300	-	-	-	100	20.0	0.02	61
	786	17.3	35.5	0.03	82.7	19.4	0.04	65
	800	39.5	35.4	0.02	60.5	17.5	0.03	67
	935	59.7	35.3	0.03	40.3	14.2	0.02	31
4	300	-	-	-	100	18.9	0.03	61
	794	16.1	35.3	0.03	83.9	17.8	0.05	63
	810	33.8	35.4	0.03	66.2	16.0	0.04	55
	935	56.3	35.3	0.03	43.7	13.6	0.04	37

Figure captions

Fig. 1. DSC scans at 10 K/min.

Fig. 2. TMG scans at 10 K/min.

Fig. 3. Local Avrami exponent from different isothermal TMG data along that

calculated applying the isokinetic approach to a DSC scan at 10 K/min.

Fig. 4. Activation energy as a function of the transformed fraction of the

nanocrystallization process.

Fig. 5. Local Avrami exponent using the isokinetic approach at different heating rates.

Fig. 6. Avrami exponent as a function of T from Ozawa method and from isokinetic

approach.

Fig. 7. XRD patterns of samples heated up to different devitrification stages.

Fig. 8. TEM images of samples heated up to different devitrification stages.

Fig. 9. A closer view of the bright field image of a 4 at. % Mn sample heated up to 810

K.

Fig. 10. Mössbauer spectra and *HF* distributions of as-cast samples.

Fig. 11. Mössbauer spectra of nanocrystalline samples of the studied alloys.

Fig. 12. *HF* distributions of nanocrystalline samples of the studied alloys.

Figure 1
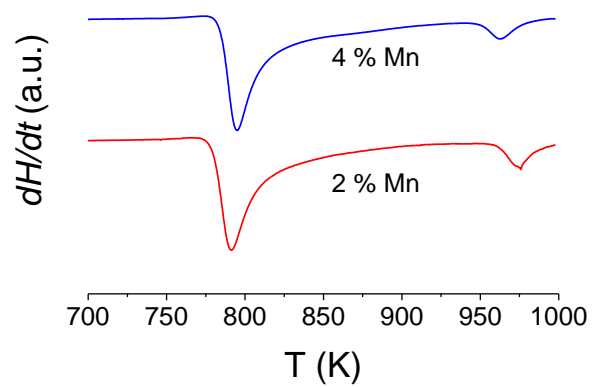
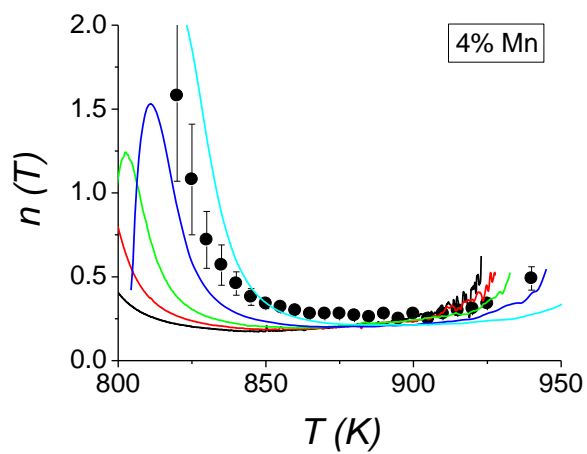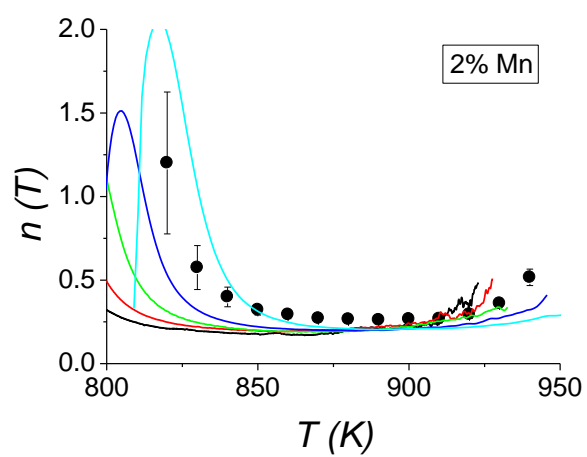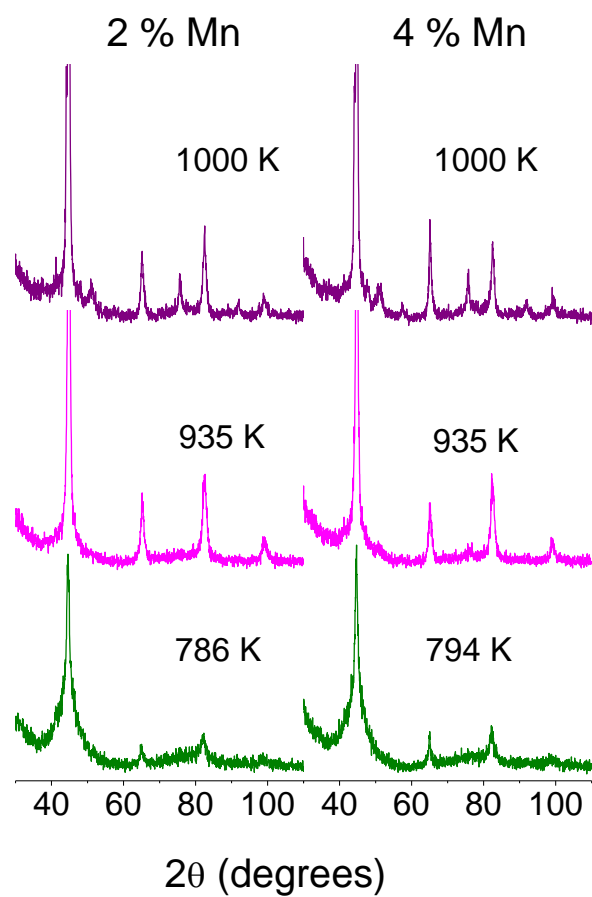Figure 2
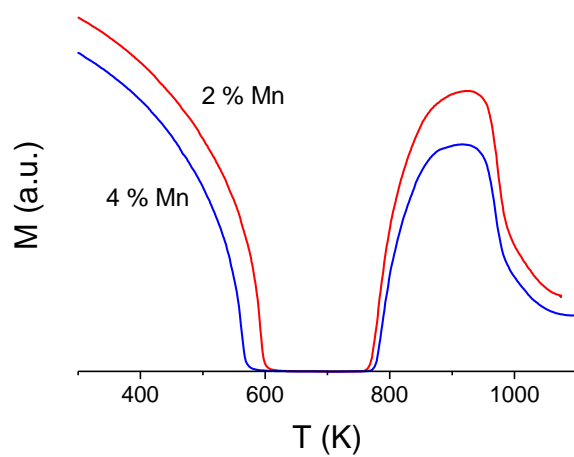
Figure 3
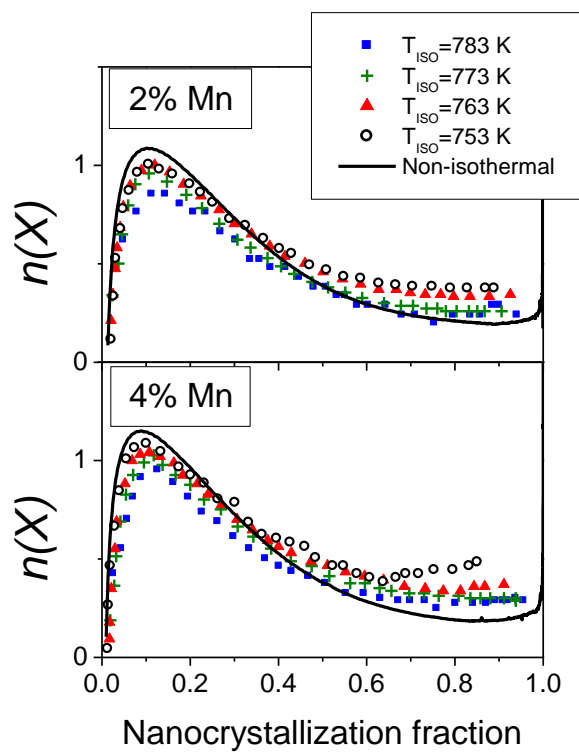
Figure 4
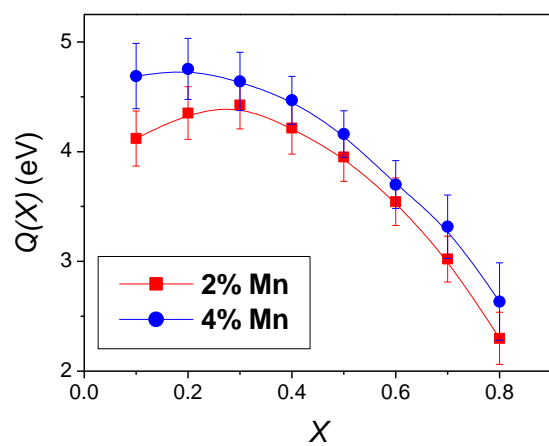
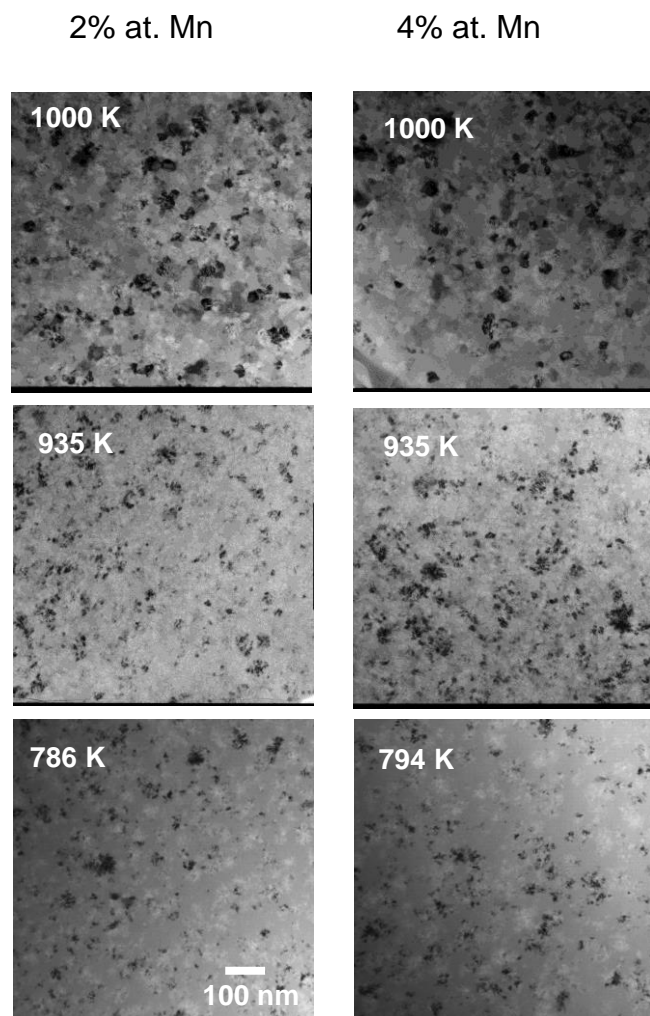Figure 5
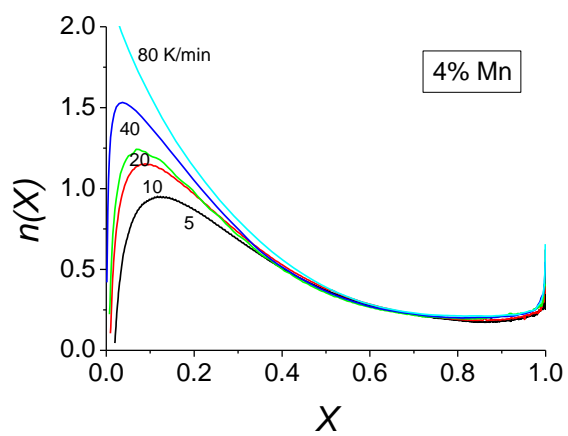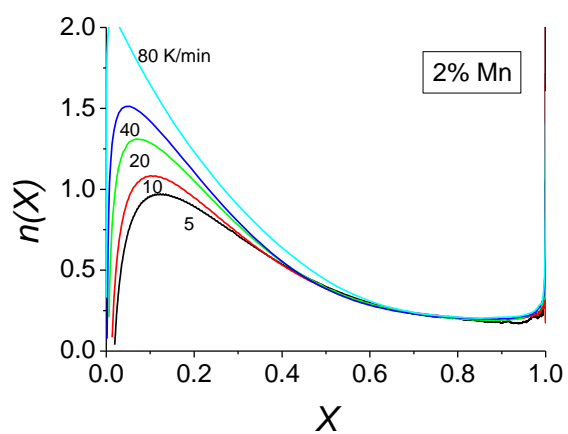
Figure 6

Figure 7

Figure 8

2% at. Mn   4% at. Mn

Figure 9

50 nm

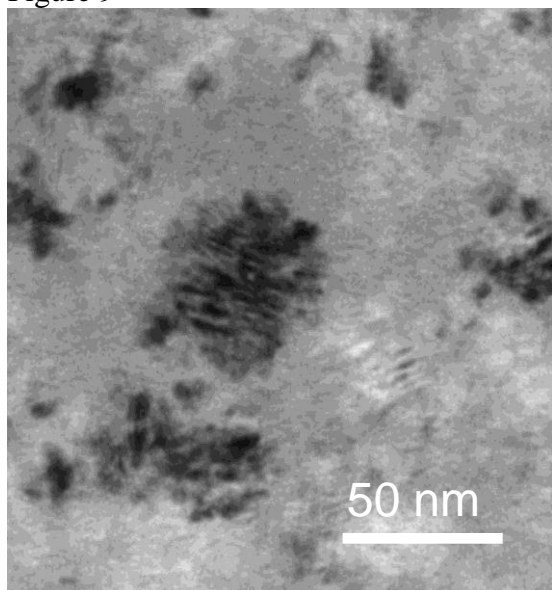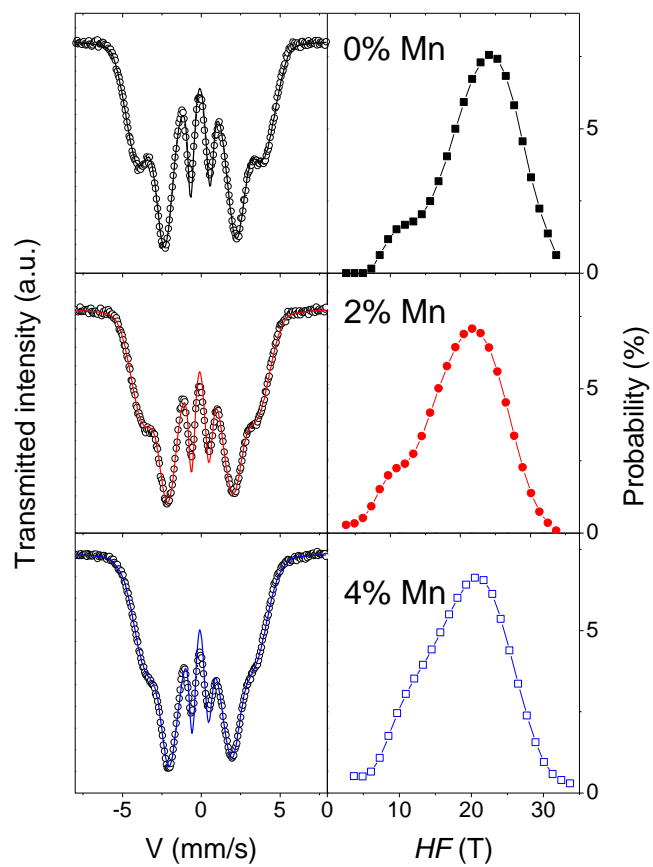Figure 10

Figure 11

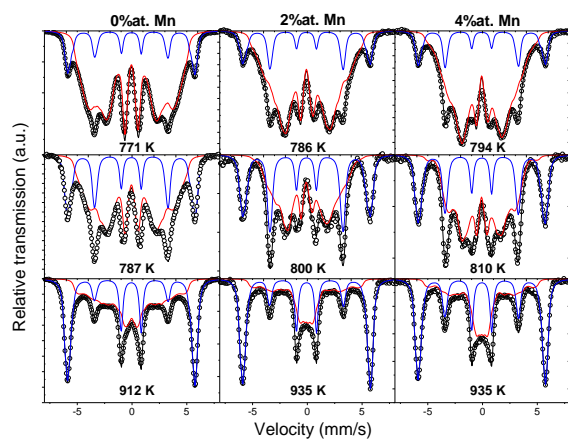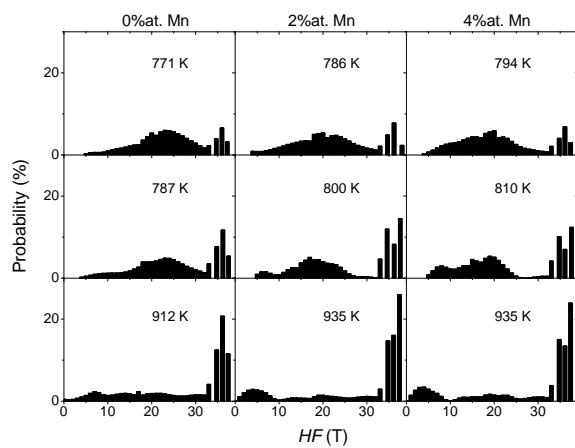Figure 12

References

[1] M. E. McHenry, M. A. Willard and D. E. Laughlin, Prog. Mater. Sci. 44 (1999) 291.

[2] A. Hernando, M. Vázquez, T. Kulik and C. Prados, Phys. Rev. B 51 (1995) 3581.

[3] M. A. Willard, D. E. Laughlin, and M. E. McHenry, J. Appl. Phys. 84 (1998) 6773.

[4] M. Müller, H. Grahl, N. Mattern, U. Kühn and B. Schnell, J. Magn. Magn. Mat.

160 (1996) 284.

[5] P. Marín, L. Pascual, A. Hernando, and M. Vázquez, Phys. Rev. B 65 (2002)

024433.

[6] J. S. Blázquez, J. M. Borrego, C. F. Conde, A. Conde and J. M. Greneche, J.Phys. :

Condens. Matter

15 (2003) 3957.

[7] C. Gomez-Polo, J.I. Pérez-Landazábal, V. Recarte, P. Mendoza Zélis, Y.F. Li and

M. Vazquez,

J. Magn. Magn. Mater 290-291 (2005) 1517.

[8] A.C. Hsiao, M.E. McHenry, D.E.Laughlin, M.R Tamoria, V.G. Harris, IEEE Trans.

Magn. 37 (2001) 2236.

[9] M.R. Tamoria, E.E. Carpenter, M.M. Miller, J.H. Claassen, B.N. Das, R.M. Stroud,

L.K. Kurihara, R.K Everett, M.A Willard, A.C. Hsiao, M.E McHenry, V.G Harris,

IEEE Trans Magn. 37 (2001) 2264.

[10] A. K. Panda, I. Chattoraj and A. Mitra, J. Magn. Magn. Mater. 222 (2000) 263.

[11] T. Bitoh, M. Nakazawa, A. Makino, A. Inoue and T. Masumoto, J. Appl. Phys.

85 (1999) 5127.

[12] M. Hasiak, M. Miglierini, Y. Yamashiro, W. H. Ciurzynska, T. Yanai and H.

Fukunaga, J. Magn. Magn. Mater. 254-255 (2003) 457.

[13]   C. F. Conde, A. Conde, P. Svec and P. Ochin, Mat. Sci. Eng. A 375-377 (2004) 718.

[14]   C. F. Conde, V. Franco, A. Conde and L. F. Kiss, J. Magn. Magn. Mater. 272-276 (2004) 1430.

[15]   J. S. Blázquez , C. F. Conde , A. Conde and J. M. Grenèche, J. All. Compd. 370 (2004) 36.

[16]   R. A. Brand, J. Lauer and D. M. Herlach, J. Phys. F: Met. Phys. 12 (1983) 675.

[17]   J.S. Blázquez, C.F. Conde, A. Conde , J. Non Cryst. Solids 287 (2001) 187.

[18]   J.S. Blázquez, C.F. Conde, A. Conde, Appl. Phys. Lett 79 (2001) 2898

[19]   J. W. Christian in: The Theory of Transformation in Metals and Alloys, Part 1, Pergamon, Oxford, 1975, p.542

[20]   J.S. Blázquez, C.F. Conde and A. Conde, Appl. Phys. A 76 (2003) 571.

[21]   J.S. Blázquez, C.F. Conde and A. Conde, Acta Mater. 53 (2005) 2305

[22]   J.S. Blázquez, V. Franco, A. Conde, J. Phys.: Cond. Matter 14 (2002) 11717.

[23]   H. H. Hamdeh, J. Okamoto, and B. Fultz, Phys. Rev. B 42 (1990) 6694.

[24]   Y. Zhang, J. S. Blazquez, A. Conde, Paul J. Warren and A. Cerezo, Mat. Sci. Eng. A 353 (2003) 158.

[25]   S.M. Cotes, A.F. Cabrera, L.C. Damonte, R.C. Mercader, J. Desimoni, *Physica B: Condensed Matter, Volume 320, Issues 1-4, July 2002, Pages 274-277*

[26]   M. Uhrmacher, A. Kulinska, Y.U.V. Baldokhin, V.V. Tcherdyntsev, S.D. Kaloshkin, A. Maddalena, G. Principi, Intermetallics 10 (2002) 571.

[27]   J.S. Blázquez, V. Franco and A. Conde, J. Alloys Compd. 422 (2006) 32.